COMPUTATION OF A SHRINKING INTERFACE IN A HELE-SHAW CELL*

MENG ZHAO†¶, XIAOFAN LI†, WENJUN YING‡, ANDREW BELMONTE§, JOHN LOWENGRUB¶, AND SHUWANG LI†

Abstract. In this paper, we present an adaptive rescaling method for computing a shrinking interface in a Hele-Shaw cell with a time increasing gap width b(t). We focus our study on a onephase interior Hele-Shaw problem where a blob of fluid, surrounded by air, dynamically responds to the changing gap width. Linear analysis suggests that there exist transient fingering instabilities and noncircular self-similar evolutions depending on the dynamics of the gap b(t). Using linear theory, we identify a critical dynamic gap thickness $b_{c_k}(t)$ that separates stable shrinking behavior (shrinkage like a circle) from unstable shrinkage (shrinkage like a fingering pattern), where k is the wavenumber of the perturbation. The gap b_{c_k} tends to infinity at a finite time. To explore the full nonlinear interface dynamics, we develop a spectrally accurate boundary integral method in which a new time and space rescaling is implemented. In the rescaled frame, the motion of the interface is slowed down, while the area/volume enclosed by the interface remains unchanged. This method, for the first time, enables us to adaptively remove the severe numerical stiffness imposed by the rapidly shrinking interface (especially at late times) and accurately compute the dynamics to far longer times than could previously be accomplished. Numerical tests demonstrate that the method is stable, efficient, and accurate. We perform nonlinear simulations for different dynamics of gap widths and, while the transient interface dynamics can be very complex, we find behavior generally consistent with the predictions of linear theory regarding the critical gap width. In particular, we find that when the b(t) increases exponentially in time, the nonlinear interface undergoes transient and sometimes dramatic morphological instabilities but eventually shrinks as a circle. When $b = b_{c_k}$, or larger gap widths are used, our simulations reveal that at long times, the interface exhibits novel, strikingly thin k-fold morphologies that do not vanish as the interface shrinks, suggesting there exists mode selection in the nonlinear regime though the evolution is not self-similar.

Key words. shrinking interface, rescaling scheme, boundary integral method, fingering instability, Hele-Shaw

AMS subject classifications. 45B05, 76S05, 76D27, 35R37

DOI. 10.1137/18M1172533

1. Introduction. In the classical radial Hele-Shaw problem, a less viscous fluid is injected into a more viscous fluid confined in a fixed narrow gap between two parallel plates. During injection, the inner less viscous fluid displaces the outer viscous fluid and the interface separating the two fluids exhibits fingering patterns due to the Saffman–Taylor instability [42]. In particular, the tip of a finger may split and develop

B1206

^{*}Submitted to the journal's Computational Methods in Science and Engineering section February 26, 2018; accepted for publication (in revised form) June 15, 2018; published electronically August 30, 2018.

http://www.siam.org/journals/sisc/40-4/M117253.html

Funding: The third author's work was supported by the National Science Foundation of China, Division of Mathematical Sciences (NSF-DMS), grant DMS-11771290. The fifth author's work was supported by NSF-DMS grants DMS-1719960 and DMS-1720420 and by NIH grant P50GM76516 for a Center of Excellence in Systems Biology at the University of California, Irvine. The sixth author's work was supported by NSF-DMS grants DMS-1720420 and ECCS-1307625.

[†]Department of Applied Mathematics, Illinois Institute of Technology, Chicago, IL 60616 (mzhao8@hawk.iit.edu (former), lix@iit.edu, sli@math.iit.edu).

[‡]School of Mathematical Sciences, Shanghai Jiaotong University, Shanghai 200240, China (wying@sjtu.edu.cn).

[§]W. G. Pritchard Laboratories, Department of Mathematics, Pennsylvania State University, University Park, PA 16802 (andrew.belmonte@gmail.com).

[¶]Department of Mathematics, University of California at Irvine, Irvine, CA 92697 (lowengrb@math.uci.edu, mzhao9@uci.edu (current)).

into new fingers. The repetition of this process leads to dense branching morphologies [42, 39, 33, 6, 29, 8, 36, 3].

Besides the classical Hele-Shaw setup, there are several variants related to the viscous fingering problem [37, 21, 20, 4, 12, 14, 13, 40]. For example, Hele-Shaw cells where the top plate is lifted uniformly at a prescribed speed and the bottom plate is fixed (lifting plate problem) [5, 12, 35, 43, 47, 45, 46] have been used to study adhesion related problems such as debonding [16, 2, 38, 11] and the associated probe tack test [51, 25]. In the lifting plate problem, the gap b(t) between the two plates is increasing in time but uniform in space. As the plate is pulled, an inner viscous fluid shrinks in the center plane between the two plates and increases in the z-direction to preserve volume. An outer less viscous fluid invades the cell and generates fingering patterns. The patterns are visually similar to those in the classical radial Hele-Shaw problem, but the driving physics is different in the sense that the flow in this problem is extensional (e.g., free-surface instabilities seen in [32]). Using linear stability theory and weakly nonlinear analysis, [12] related the rate of change of the gap width with the number of developing fingers and derived a critical rate that selects the number of fingers observed and obtained good agreement with experiments [13]. Similar results are observed using a Hele-Shaw cell with one edge of the plate lifted, which makes the gap width a function of time and space [48, 14].

There are two numerical issues when computing the nonlinear dynamics of a shrinking interface. The first challenge is that one has to solve a stiff dynamical system. The stiffness comes from the fast dynamics of the interface when the top plate is lifted rapidly (e.g., an exponentially increasing gap $b(t) = \exp(t)$ for large t), which requires a significant reduction in time steps to maintain the accuracy and stability of long-time computations. The second difficulty is, as the interface shrinks and develops complex fingering patterns, one may have to increase the spatial resolution (e.g., by adding more mesh points) to resolve the interface, which again compounds the temporal resolution and demands even smaller time steps. Explicit time stepping methods suffer from a third order time step constraint $\Delta t \sim \Delta s^3$, where Δs is the arclength spacing between computational nodes along interface. These severe time step constraints substantially increase the computational cost and make long-time computations prohibitive in practice.

To overcome these difficulties, we develop a spectrally accurate boundary integral method in which a new time and space rescaling is implemented. The rescaling idea [29, 49, 50] is to map the original time and space (\mathbf{x},t) into new coordinates $(\bar{\mathbf{x}},\bar{t})$ such that the interface can evolve at an arbitrary speed in the new rescaled frame. In particular, for the shrinking interface problem, we choose (1) the space scaling function $R(\bar{t})$ so that the shrinking interface is always mapped back to its initial size, i.e., the interface does not shrink in the rescaled frame; (2) the time scaling function $\rho(\bar{t})$ to slow down the motion of the interface, especially at later times when the interface becomes very small and shrinks extremely rapidly. We note that an alternative time and space rescaling scheme was implemented in [9, 10] to accurately simulate vanishing bubbles in a Hele-Shaw cell. Here, we use a semi-implicit, nonstiff time stepping method developed originally in [23] to remove the third order time step constraint. The slow interface dynamics in the rescaled frame, together with the nonstiff time stepping method, allows one to use large time steps in calculations, which solves the temporal stiffness issue. For example, the original exponentially increasing gap $b(t) = \exp(t)$ may be slowed down to $b(\bar{t}) = 1 + 0.5\bar{t}$ in the new frame.

To provide insight to the problem, we revisit the linear stability analysis of a slightly perturbed circular interface. We identify a dynamic, critical gap thickness $b_{c_k}(t) = (1 - \frac{7}{2}c_kt)^{-2/7}$ that separates unstable and stable shrinkage of perturbations with wavenumber k and $c_k \sim k^2$. That is, linear theory predicts that when $\frac{d}{dt}(\frac{1}{b_{c_k}^{7/2}} - \frac{1}{b^{7/2}}) < 0$ mode k shape perturbations will eventually decrease in time while for $\frac{d}{dt}(\frac{1}{b_{c_k}^{7/2}} - \frac{1}{b^{7/2}}) > 0$ mode k perturbations will increase as the interface shrinks. When $b = b_{c_k}$, the perturbation evolves self-similarly. Note that $b_{c_k}(t)$ becomes unbounded at a finite time.

For more slowly increasing gaps, such as those that linearly or even exponentially increase in time, we identify a critical time t^* such that after t^* the perturbation starts to decay. Before the critical time t^* , nonlinear simulations reveal that the interfaces may show dramatic, transient fingering instabilities. For instance, under such conditions the interfaces develop multiple fingers and new modes arise as the interface shrinks initially. However, unlike fingering patterns observed in the classical Hele-Shaw problem, here the number of fingers decreases over time and the fingers do not split during evolution. After the critical time, the fingers decay and the interface tends to a circle as it vanishes, consistent with predictions from linear theory.

From linear theory, we also derive a mode selection criterion based on the mode with the maximum growth rate k_{max} and the mode with the maximum perturbation amplitude k^* . Defining a more general gap dynamics $b_c(t) = \left(1 - \frac{7}{2}c \cdot t\right)^{-2/7}$ we may select k_{max} or k^* by taking different values of c. Using these rapidly increasing gaps, nonlinear results reveal that at long times the interfaces exhibit nontrivial k-mode dominant morphologies, suggesting there also exists a mode selection mechanism in the nonlinear regime. In these cases, the interface does not seem to tend to a circle as it vanishes.

In [43], the authors constructed a so-called fission interface (two connected circles) that would split into two separate circles in the absence of surface tension. For a finite surface tension, short-time simulations using $b(t) = \exp(t)$ show that the fission interface might split at the center of the channel region [43], which would be in agreement with the lubrication approximation for flows in a thin channel [1]. Note that in the lubrication approximation, the interface is assumed to be smooth and no fingers develop. Here, our nonlinear simulations demonstrate that the neck region of the fission interface develops multiple fingers and that the interface ultimately shrinks like a circle even for a small surface tension. We find that the fission interface experiences four dynamical stages as it shrinks: Dumbbell Stage I, Fingering Stage, Dumbbell Stage II, and Circular Stage.

This paper is organized as follows: in section 2, we present the governing equations and linear stability analysis; in section 3, we develop a rescaled boundary integral method; in section 4, we discuss the numerical results; and in section 5, we give conclusions and discuss future work.

2. Governing equations and linear analysis. We consider a radial Hele-Shaw cell with a time dependent gap b(t); see Figure 1 for a schematic plot. The upper plate is lifted perpendicularly to the cell, while the lower plate stays fixed. The interior fluid (e.g., oil) meets with the exterior less viscous fluid (e.g., air) at the interface $\partial\Omega$. Assuming that the two fluids are immiscible and incompressible, we have the following governing equations [43]:

$$\mathbf{u} = -\frac{b^2(t)}{12\mu} \nabla P \quad \text{in } \Omega \subset \mathbb{R}^2,$$

(2.2)
$$\nabla \cdot \mathbf{u} = -\frac{\dot{b}(t)}{b(t)} \quad \text{in } \Omega \subset \mathbb{R}^2,$$

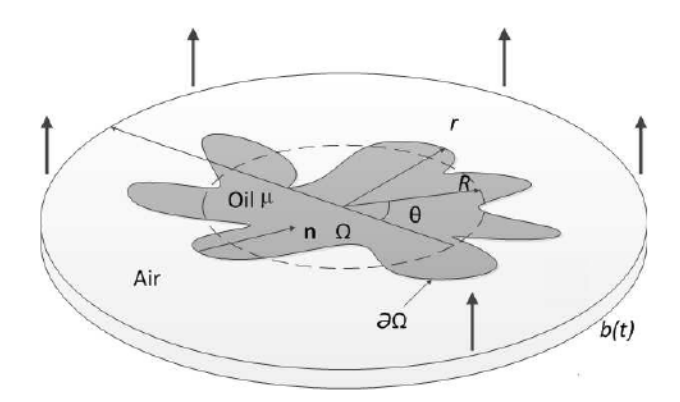


Fig. 1. Schematic for the lifting plate Hele-Shaw problem. The interior region Ω is oil with viscosity μ . The exterior region is air. b(t) is the time dependent gap. The normal n to the interface $\partial\Omega$ points inward.

(2.3)
$$[P]_t = \tau \kappa \quad \text{on} \quad \partial \Omega \subset \mathbb{R}^2,$$

(2.4)
$$V = -\frac{b^2(t)}{12\mu} \frac{\partial P}{\partial \mathbf{n}} \quad \text{on} \quad \partial \Omega \subset \mathbb{R}^2.$$

Equation (2.1) follows from Darcy's law, where u is the velocity, P is the pressure, and μ is the viscosity of the fluid. Equation (2.2) is the gap-averaged incompressibility condition that reflects the conservation of fluid volume, where $\dot{b}(t) = \frac{db(t)}{dt}$ is the lifting speed. Equation (2.3) is the boundary condition, where the pressure jump $[P]_t$ across the interface is given by the product of surface tension τ and the curvature of the interface κ , known as the Laplace–Young condition. Equation (2.4) describes the normal velocity of the interface V and \mathbf{n} is the unit normal vector pointing inward. See [26, 17] for a derivation of this system.

Using the equivalent radius of the initial interface L_0 as the length scale (radius of a circle with the same enclosed area), the characteristic time $T = \frac{b_0}{\dot{b}_0}$ as the time scale, the pressure $P_0 = \frac{12\mu L_0^2}{Tb_0^2}$ as the pressure scale, where b_0 and \dot{b}_0 are the initial values of b and \dot{b} . Defining the nondimensional surface tension as $\tau_0 = \frac{\tau b_0^3}{12\mu \dot{b}_0 L_0^3}$, the nondimensional version of (2.1), (2.2), (2.3), and (2.4) is

(2.5)
$$\mathbf{u} = -b^2(t)\nabla P \quad \text{in } \Omega,$$

(2.6)
$$\nabla \cdot \mathbf{u} = -\frac{\dot{b}(t)}{b(t)} \quad \text{in } \Omega,$$

(2.7)
$$\nabla^2 P = \frac{\dot{b}(t)}{b^3(t)} \quad \text{in } \Omega,$$

(2.8)
$$[P]_t = \tau \kappa \quad \text{on} \quad \partial \Omega,$$

(2.9)
$$V = -b^{2}(t)\frac{\partial P}{\partial \mathbf{n}} \quad \text{on} \quad \partial \Omega,$$

where we have retained the same notation as before but now b(0) = 1 and $\tau = \tau_0$. Following [43], we define a harmonic function $\tilde{P} = P - \frac{\dot{b}(t)}{4b^3(t)}|\mathbf{x}|^2$ and rewrite (2.7), (2.8), and (2.9) as

(2.10)
$$\nabla^2 \tilde{P} = 0 \quad \text{in } \Omega,$$

(2.11)
$$[\tilde{P}]_t = \tau \kappa - \frac{\dot{b}(t)}{4b^3(t)} |\mathbf{x}|^2 \quad \text{on} \quad \partial \Omega,$$

$$\tilde{V} = -b^2(t) \frac{\partial \tilde{P}}{\partial \mathbf{n}} \quad \text{on} \quad \partial \Omega.$$

That is, the new normal velocity is given by

(2.13)
$$\tilde{V} = V + \frac{\dot{b}(t)}{2b(t)} \mathbf{x} \cdot \mathbf{n}.$$

Linear stability analysis. We consider the interface to be a slightly perturbed circle, $r(\alpha, t) = R(t) + \epsilon \delta(t) \cos(k\alpha)$, where $\epsilon \ll 1$, the perturbation mode $k \geq 2$ is an integer, $\alpha \in [0, 2\pi]$ is the polar angle, and $\delta(t)$ is the amplitude of the perturbation.

Following standard perturbation analysis and using the volume conservation of the viscous fluid (the nondimensional volume is π) [13, 43], we have $\frac{\dot{R}}{R} = -\frac{\dot{b}}{2b}$ and $\frac{\dot{\delta}}{\delta} = \frac{\dot{b}(k-1)}{2b} - \tau \frac{b^2(k^3-k)}{R^3}$. We define the shape factor $\frac{\delta}{R}$ to characterize the evolution of the perturbation [34],

(2.14)
$$\left(\frac{\delta}{R}\right)^{-1} \frac{d}{dt} \left(\frac{\delta}{R}\right) = \frac{\dot{b}k}{2b} - \tau \frac{b^2(k^3 - k)}{R^3}.$$

Equation (2.14) is the linear growth rate of the kth mode perturbation. Using the relationship $R = 1/\sqrt{b}$ from volume conservation and nondimensionalization, we can rewrite (2.14) as

$$\left(\frac{\delta}{R}\right)^{-1} \frac{d}{dt} \left(\frac{\delta}{R}\right) = \frac{1}{7} k \cdot b^{7/2} \frac{d}{dt} \left(\frac{1}{b_{c_k}^{7/2}} - \frac{1}{b^{7/2}}\right),$$

where b_{c_k} is the critical gap that satisfies

(2.16)
$$\frac{\dot{b}_{c_k}}{b_{c_k}^{9/2}} = 2\tau \left(k^2 - 1\right),$$

or equivalently,

(2.17)
$$b_{c_k}(t) = \left(1 - \frac{7}{2}c_k \ t\right)^{-2/7} \text{ with } c_k = 2\tau \left(k^2 - 1\right).$$

This critical gap $b_{c_k}(t)$ was also derived in [12]. Observe that perturbations grow (or decay) when

$$\frac{d}{dt}\left(\frac{1}{b_{c_k}^{7/2}} - \frac{1}{b^{7/2}}\right)$$

is positive (or negative). When $b = b_{c_k}$, the shape perturbation is unchanged in time, that is, the configuration is a dynamical equilibrium state (linear self-similar solution) [29, 30, 28]. Note that the time dependent gap in (2.17) only exists for a finite time $T_k = \frac{2}{7c_k}$. The gap increases slowly at early times, but as t approaches T_k , the gap grows rapidly and becomes unbounded.

Solving (2.14), or equivalently (2.15), we obtain

(2.18)
$$\frac{\delta}{R}(t) = \left(\frac{\delta}{R}\right)_0 b^{\frac{k}{2}}(t) e^{\sigma(k) \int_0^t b^{7/2}(s) ds},$$

where $\left(\frac{\delta}{R}\right)_0$ is the initial perturbation, and $\sigma(k) = \tau(k - k^3)$. We have the following results.

STATEMENT 2.1. For any mode k, if $\frac{d}{dt}(\frac{1}{b^{7/2}} - \frac{1}{b^{7/2}})$ changes sign from positive at early times to negative at late times, then there is a critical time t^* after which $\frac{\delta}{R}(t)$ starts to decay. The critical time t^* is characterized by

$$\dot{b}(t^*) = \beta(k)b^{9/2}(t^*),$$

where $\beta(k) = \frac{-2\sigma(k)}{k}$. Further, if $b(t) \to +\infty$ as $t \to +\infty$, then for all s > 0, $\frac{\delta}{R}(t) \sim o(b^{-s}(t))$ as $t \to +\infty$.

To find the critical time t^* , we set the right-hand side of (2.15) to be zero. The result $\dot{b}(t^*) = \beta(k)b^{9/2}(t^*)$, where $\beta(k) = 2\tau(k^2 - 1)$, immediately follows. Since $b(t) \to +\infty$ as $t \to +\infty$, we conclude $\dot{b}(t) \sim o(b^{1+\epsilon_1}(t))$ as $t \to +\infty$ for any $\epsilon_1 > 0$. If $\dot{b}(t) \sim O(b^{1+\epsilon_1}(t))$, then $b(t) \sim O((1-\epsilon_1ct)^{-1/\epsilon_1})$. It indicates b(t) goes unbounded at a finite time, which is in contradiction with $b(t) \to +\infty$ as $t \to +\infty$. Then we have $\dot{b}(t) \sim o(b^{1+\epsilon_1}(t))$ as $t \to +\infty$ for any $\epsilon_1 > 0$. Using (2.18), we have

$$\begin{split} \lim_{t \to \infty} \frac{\frac{\delta}{R}(t)}{b^{-s}(t)} &= \left(\frac{\delta}{R}\right)_0 \lim_{t \to \infty} \frac{b^{\frac{k}{2} + s}(t)}{e^{-\sigma(k) \int_0^t b^{7/2}(s) ds}} \\ &= \left(\frac{\delta}{R}\right)_0 \lim_{t \to \infty} \frac{b^{\frac{k}{2} + s} \frac{\dot{b}}{b^{9/2}}}{-\sigma(k) e^{-\sigma(k) \int_0^t b^{7/2}(s) ds}} \\ &= \left(\frac{\delta}{R}\right)_0 \lim_{t \to \infty} \frac{b^{\frac{k}{2} + s} o(b^{\epsilon_1 - 7/2})}{-\sigma(k) e^{-\sigma(k) \int_0^t b^{7/2}(s) ds}} \\ &= 0. \end{split}$$

The second equality comes from l'Hôpital's rule. The last equality is due to $b^{\frac{k}{2}+s}o(b^{n(\epsilon_1-7/2)})$ approaching zero after repeating l'Hôpital's rule finite number n times.

For linearly and exponentially increasing time dependent gaps, the perturbation grows at early times. After the critical time t^* , the perturbation starts to decay, and the interface eventually tends to a circle as it vanishes. This has been observed in experiments [31, 2, 11].

Statement 2.2. The maximum growth rate mode k_{max} is

(2.20)
$$k_{max} = \sqrt{\frac{\dot{b}}{6\tau b^{9/2}} + \frac{1}{3}},$$

and associated gap $b(t) = \left(1 - \frac{7}{2}ct\right)^{-2/7}$ with $c = 2\tau \left(3k^2 - 1\right)$. The mode k^* with the maximum perturbation amplitude is given by

(2.21)
$$k^* = \sqrt{\frac{\ln b(t)}{6\tau \int_0^t b^{7/2}(s)ds} + \frac{1}{3}}.$$

If b(t) is a linear or exponential function of time, then both k_{max} and k^* tend to $\sqrt{1/3}$ as $t \to +\infty$.

We find the maximum growth rate mode by setting

$$\frac{d}{dk} \left[\left(\frac{\delta}{R} \right)^{-1} \frac{d}{dt} \left(\frac{\delta}{R} \right) \right] = 0$$

and solving for k_{max} . We get the maximum perturbation amplitude mode by taking the derivative of (2.18) with respect to k, then using $\frac{d(\frac{\delta}{R})}{dk} = 0$ to solve for k^* . It is straightforward to verify that for linearly or exponentially increasing gaps b(t), k_{max} and k^* tend to $\sqrt{1/3}$ as $t \to +\infty$.

Recalling that k_{max} and k^* are integers (perturbation modes), the limit value $\sqrt{1/3}$ merely implies the interface eventually reduces to a circle. Usually, k_{max} and k^* are different and there are two different criteria for mode selection in a nonequilibrium state. One is the commonly used k_{max} criterion, which has been shown to provide a good estimate of the number of growing fingers [35]. The other is the k^* criterion, which shows agreement with experimental data on the total number of fingers [13].

3. Numerical method and rescaling.

3.1. Boundary integral formulation. The reduced pressure \tilde{P} is harmonic. From potential theory, we can write \tilde{P} as a double layer integral,

$$\tilde{P}(\mathbf{x}) = \int_{\partial\Omega} \tilde{\gamma}(\mathbf{x}') \left[\frac{\partial \ln |\mathbf{x} - \mathbf{x}'|}{\partial \mathbf{n}(\mathbf{x}')} + 1 \right] ds(\mathbf{x}'),$$

where $\tilde{\gamma}(\mathbf{x})$ is the dipole density on $\partial\Omega$. Assuming the exterior fluid is air, we only need to solve the interior fluid problem. Using the boundary condition, $\tilde{\gamma}$ satisfies a Fredholm integral equation of the second kind,

(3.1)
$$\tilde{\gamma}(\mathbf{x}) + \frac{1}{\pi} \int_{\partial \Omega} \tilde{\gamma}(\mathbf{x}') \left[\frac{\partial \ln |\mathbf{x} - \mathbf{x}'|}{\partial \mathbf{n}(\mathbf{x}')} + 1 \right] ds(\mathbf{x}') = 2\tau \kappa - \frac{\dot{b}(t)}{2b^3(t)} |\mathbf{x}|^2,$$

with

(3.2)
$$\int_{\partial\Omega} \tilde{\gamma}(\mathbf{x}) ds(\mathbf{x}) = 0.$$

This is a well-conditioned problem that can be solved efficiently using an iterative method such as GMRES [41]. Once we obtain $\tilde{\gamma}$, the normal velocity \tilde{V} can be computed via the Dirichlet–Neumann map [18]:

(3.3)
$$\tilde{V}(t) = -\frac{b^2(t)}{2\pi} \int_{\partial \Omega} \tilde{\gamma}_{s'} \frac{(\mathbf{x}' - \mathbf{x})^{\perp} \cdot \mathbf{n}}{|\mathbf{x}' - \mathbf{x}|^2} ds',$$

where $\mathbf{x}^{\perp} = (x_2, -x_1)$. Using (2.13) we have the normal velocity of the interface,

(3.4)
$$V(t) = -\frac{b^2(t)}{2\pi} \int_{\partial\Omega} \tilde{\gamma}_{s'} \frac{(\mathbf{x}' - \mathbf{x})^{\perp} \cdot \mathbf{n}}{|\mathbf{x}' - \mathbf{x}|^2} ds' - \frac{\dot{b}}{2b} \mathbf{x} \cdot \mathbf{n}.$$

Notice that $V(t) \sim b^2(t)$. In particular, for the case $b(t) = (1 - \frac{7}{2}ct)^{-\frac{2}{7}}$, we have $b(t) \to +\infty$ as time approaches to T_k . Thus the normal velocity becomes unbounded at later times, which prohibits one from computing the dynamics of a shrinking interface as time approaches T_k . Thus, we introduce the following rescaling scheme to slow down this accelerated dynamics.

3.2. Rescaling idea. Introduce a new frame $(\bar{\mathbf{x}}, \bar{t})$ such that

$$\mathbf{x} = \bar{R}(\bar{t})\bar{\mathbf{x}}(\bar{t},\alpha),$$

$$\bar{t} = \int_0^t \frac{1}{\rho(t')} dt',$$

where the space scaling $\bar{R}(\bar{t})$ accounts for the change in size of the interface due to the gap dynamics and is determined by requiring the area in the scaled frame to be independent of time (see below). $\bar{\mathbf{x}}$ is the position vector of the scaled interface, and α parameterizes the interface. The time scaling function $\rho(t) = \bar{\rho}(\bar{t})$ maps the original time t to the new time \bar{t} and $\rho(t)$ has to be positive and continuous. The evolution of the interface in the scaled frame can be accelerated [50, 49] or decelerated by choosing a different $\rho(t)$. A straightforward calculation shows the normal velocity in the new frame

(3.7)
$$\bar{V}(\bar{t}) = \frac{\bar{\rho}}{\bar{R}}V(t(\bar{t})) - \frac{\bar{\mathbf{x}} \cdot \mathbf{n}}{\bar{R}}\frac{d\bar{R}}{d\bar{t}},$$

where V is the normal velocity in original frame. In the scaled frame, we require the area enclosed by the interface is a constant, i.e., $\bar{A}(\bar{t}) = \bar{A}(0)$. In particular, this means that the integration of the normal velocity \bar{V} along the interface in the scaled frame is zero, $\int_{\partial \bar{\Omega}} \bar{V} d\bar{s} = 0$. Using the volume conservation condition of the viscous fluid, we have

(3.8)
$$\bar{R}^{-1}\frac{d\bar{R}}{d\bar{t}} = -\frac{\bar{\rho}\dot{b}(t(\bar{t}))}{2b(t(\bar{t}))},$$

where the dot means the time derivative in the original frame. Plugging (3.8) into (3.7) and using (2.13), we have $\bar{V} = \frac{\bar{\rho}}{R} \tilde{V}(t)$.

In this paper, we consider the time dependent gap b(t) in the form of

$$\frac{\dot{b}}{b} = \alpha_1 b^l,$$

where $\alpha_1 > 0$ and l can be a positive or negative real number. In the new frame, we let the scaling factor satisfy

$$(3.10) \bar{R}^{-1} \frac{d\bar{R}}{d\bar{t}} = -\alpha_2 \bar{R}^m,$$

where $\alpha_2 > 0$ and m can be a positive or negative real number. The negative sign indicates the interface shrinks (\bar{R} decreases). Plugging (3.9) and (3.10) into (3.8), we obtain

$$\bar{\rho} = \frac{2\alpha_2}{\alpha_1} \bar{R}^{m+2l}.$$

As a result, we have

$$t = \left\{ \begin{array}{ll} \frac{1}{\alpha_1 l} (1 - \bar{R}^{2l}(\bar{t})), & l \neq 0, \\ -\frac{2}{\alpha_1} \ln \bar{R}(\bar{t}), & l = 0. \end{array} \right. \label{eq:total_total_total}$$

Note that different choices of m and α_2 lead to different evolution speeds of the interface in the new frame. For m < -2l and $\alpha_1 < 2\alpha_2$, $\bar{\rho} > 1$ indicates the evolution of the interface is accelerated in the new frame. For m > -2l and $\alpha_1 > 2\alpha_2$, $\bar{\rho} < 1$ indicates the evolution of the interface is decreased in the new frame.

Taking $\tilde{\gamma} = \bar{\gamma} \bar{R}^{-1}$, (3.1) can be rewritten as

$$(3.12) \quad \bar{\gamma}(\bar{\mathbf{x}}) + \frac{1}{\pi} \int_{\partial \bar{\Omega}(\bar{t})} \bar{\gamma}(\bar{\mathbf{x}}') \left[\frac{\partial \ln |\bar{\mathbf{x}} - \bar{\mathbf{x}}'|}{\partial \mathbf{n}(\bar{\mathbf{x}}')} + \bar{R}(\bar{t}) \right] d\bar{s}(\bar{\mathbf{x}}') = 2\tau \bar{\kappa} - \frac{\dot{b}(t(\bar{t}))}{2b^3(t(\bar{t}))} \bar{R}^3 |\bar{\mathbf{x}}|^2.$$

Using (3.7), \bar{V} can be computed as

(3.13)
$$\bar{V}(\bar{\mathbf{x}}) = -\frac{b^2(t(\bar{t}))\bar{\rho}}{2\pi\bar{R}^3} \int_{\partial\bar{\Omega}} \bar{\gamma}_{\bar{s}} \frac{(\bar{\mathbf{x}}' - \bar{\mathbf{x}})^{\perp} \cdot \mathbf{n}(\bar{s})}{|\bar{\mathbf{x}}' - \bar{\mathbf{x}}|^2} d\bar{s}',$$

where $\bar{\mathbf{x}}^{\perp} = (\bar{x}_2, -\bar{x}_1)$. Now we evolve the interface in the scaled frame through

(3.14)
$$\frac{d\bar{\mathbf{x}}(\bar{t},\alpha)}{d\bar{t}} \cdot \mathbf{n} = \bar{V}(\bar{t},\alpha).$$

Here, we focus on a scheme that slows down the evolution of the interface in the rescaled frame. For example, let us consider the specific gap $b(t) = \left(1 - \frac{7}{2}ct\right)^{-\frac{2}{7}}$, under which linear theory predicts a self-similar shrinking interface (see (2.17)). We obtain $\alpha_1 = c$ and l = 7/2 following (3.9). Then we take $\alpha_2 = 1/4$, and m = 2 to get a linear gap $\bar{b}(\bar{t}) = 1 + 0.5\bar{t}$ via a time scaling $\bar{\rho} = \bar{R}^9/2c$. As a consequence, in the rescaled frame, the normal velocity is decelerated $\bar{V}(\bar{\mathbf{x}}) = \frac{\bar{R}^2}{2c} \frac{1}{2\pi} \int_{\partial \bar{\Omega}} \bar{\gamma}_{\bar{s}} \frac{(\bar{\mathbf{x}}' - \bar{\mathbf{x}})^{\perp} \cdot \mathbf{n}(\bar{s})}{|\bar{\mathbf{x}}' - \bar{\mathbf{x}}|^2} d\bar{s}'$. In summary, we discretize (3.12) in space using a spectrally accurately discretization.

In summary, we discretize (3.12) in space using a spectrally accurately discretization following [22, 24], evaluate the integral using the fast multipole method [19], and solve for rescaled dipole density $\bar{\gamma}$ using GMRES [41]. Because (3.12) is well-conditioned, no preconditioner is needed. Once the solution $\bar{\gamma}$ is obtained, we compute (3.13) for the rescaled normal velocity \bar{V} via the Dirichlet–Neumann map [18] using a spectrally accurate discretization [22, 24, 27]. Finally we evolve the interface in the scaled frame (3.14) using a second order accurate nonstiff updating scheme in time and an equal arclength parameterization of the interface [22, 24, 27].

4. Numerical results.

4.1. Comparison with linear theory. In this section, we present a comparison of our nonlinear results with the prediction from linear analysis. Consider a shrinking air-oil interface whose initial shape is a slightly perturbed circle, $r(\alpha,0)=1+0.01\cos(4\alpha)$, where α parametrizes the interface. The upper plate of the Hele-Shaw cell is lifted exponentially rapidly $b(t)=\exp(t)$ in the original frame and is slowed down to $b(\bar{t})=1+0.5\bar{t}$ in the rescaled frame. We set N=4096 mesh points along the interface, the time step $\Delta \bar{t}=1\times 10^{-4}$, and the surface tension $\tau=4\times 10^{-5}$. To characterize the interface morphology, we compute the shape factor numerically using $\left(\frac{\delta}{R}(t)\right)_{NL}=\max_{\alpha}\left||\bar{\mathbf{x}}(\alpha,t)|/\bar{R}_{eff}-1\right|$, where $\bar{\mathbf{x}}$ is the position vector measured from the centroid of the shape to the interface, $\bar{R}_{eff}=\sqrt{\bar{A}/\pi}$ is the effective radius of the viscous fluid in the rescaled frame, and \bar{A} is the constant area enclosed by the interface.

In Figure 2, we plot the shape factor $\frac{\delta}{R}(t)$ as a function of R and show sample interface morphologies as insets. Because of the simple initial configuration and less pronounced fingering pattern, we are also able to perform a simulation using the original (unscaled) method and obtain the same numerical results as the new scaled method, as expected. From linear theory, we know the interface will first develop a fourfold fingering pattern before ultimately shrinking to a circle as it vanishes. The linear shape perturbation evolves following $\frac{\delta}{R}(t) = \left(\frac{\delta}{R}\right)_0 R^{-4}(t) \exp\left[\frac{120\tau}{7}(1 - R^{-7}(t))\right]$.

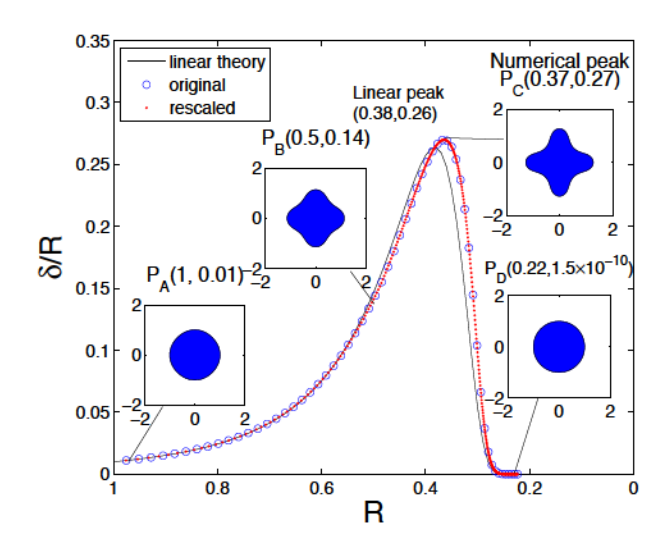


FIG. 2. Comparison between linear theory and nonlinear simulations using both the rescaled and original frames. The shape factor $\frac{\delta}{R}$ from linear theory and nonlinear simulations using $b(t) = \exp(t)$ is shown as a function of R. There are good agreements between all three. Insets show simulated interface morphologies at the indicated R.

In particular, linear theory predicts $\frac{\delta}{R}(t)$ obtains its maximum value 0.26 at R=0.38 and t=1.94, which is in good agreement with our nonlinear results, $\left(\frac{\delta}{R}\right)_{NL}=0.27$ at R=0.37 and t=1.9.

4.2. Performance of the rescaled numerical method. In this section, we test the performance of our scheme by computing the long-time nonlinear dynamics of a shrinking interface where the fingering pattern is complex and dynamic. We take the initial interface as a mode mixture, $r(\alpha,0) = 1 + 0.02(\cos(3\alpha) + \sin(7\alpha) + \cos(15\alpha) + \sin(25\alpha))$. The gap increases exponentially rapidly, $b(t) = \exp(t)$. Here we implement a time scaling factor $\rho = R^2/2$ to slow down this accelerated evolution such that in the rescaled frame, $b(\bar{t}) = 1 + 0.5\bar{t}$ and $\bar{R} = (1 + 0.5\bar{t})^{-1/2}$. From linear theory, we know that the interface will develop dynamic fingering patterns as it shrinks. The accuracy of our rescaled method is checked in a number of ways. Here we show convergence estimates, e.g., $\mathcal{O}(\Delta \bar{t}^2)$ in time and spectral accuracy in space. All simulations are performed on a single node in a cluster with 1.6 GHZ CPUs running Linux.

Convergence test. First we perform a temporal resolution study using N=8192 mesh points along the interface. We use time steps $\Delta \bar{t}=4.0\times 10^{-4}, 2.0\times 10^{-4}, 1.0\times 10^{-4}, \text{ and } 0.5\times 10^{-4}$. The surface tension $\tau=1\times 10^{-5}$. The numerical error is measured in term of the area difference in the rescaled frame, $Error=|\bar{A}(\bar{t})-\bar{A}(0)|$, where $\bar{A}(0)$ is the area enclosed by the initial interface, and $\bar{A}(\bar{t})$ is the area computed at time \bar{t} . In theory, the area difference should be zero following (3.7). In Figure 3(a), we plot the base 10 logarithm of the temporal error as a function of the scaling factor $R(t)=\bar{R}(\bar{t}(t))$, which decreases from 1 to 0.35 in these calculations. The morphologies of the interface are shown as insets, which are almost identical at the same radius for these calculations. When the time step is reduced by half, the distance between two neighboring curves decreases uniformly by a factor of 0.6 indicating the expected second order convergence in time.

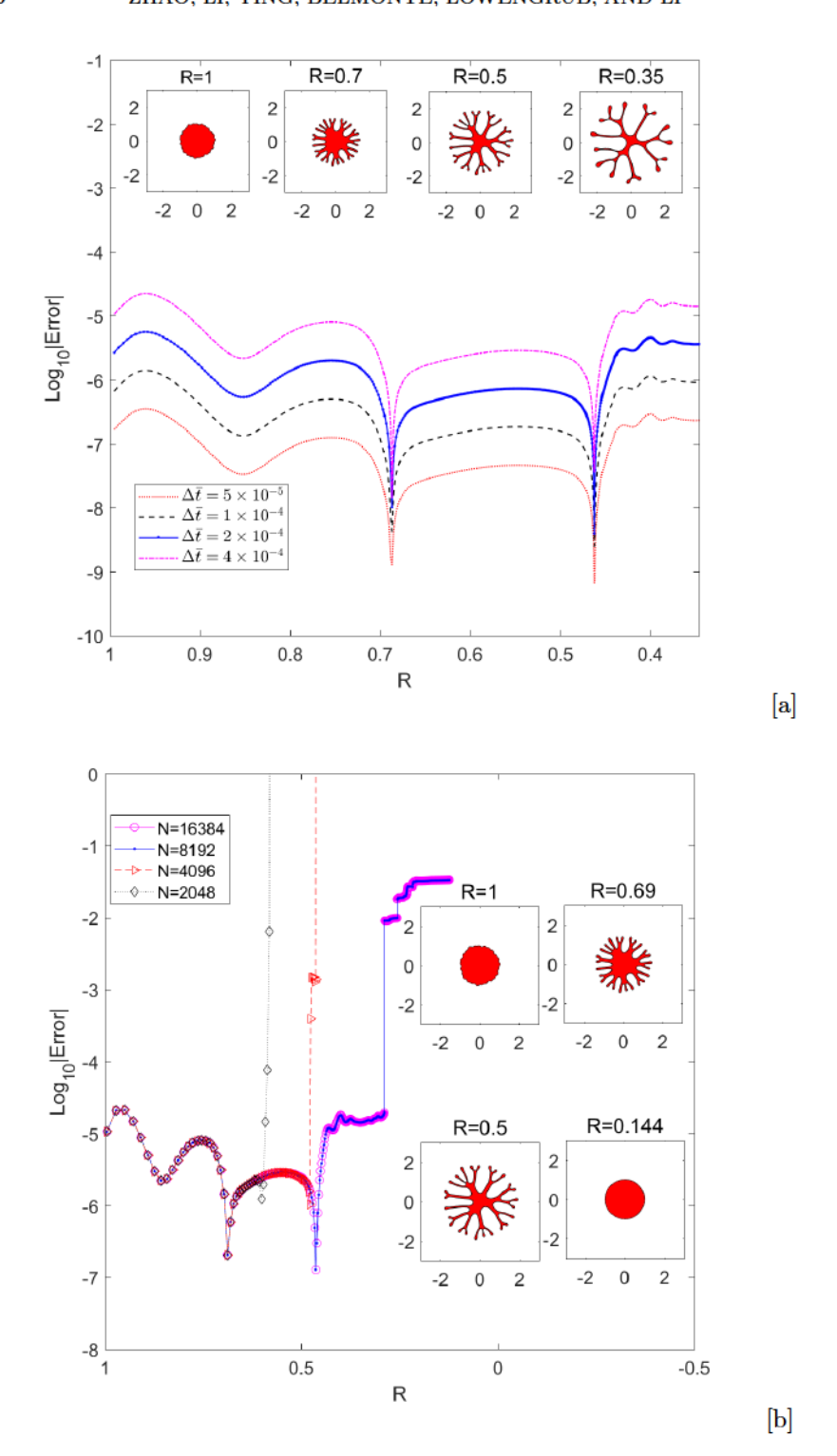


Fig. 3. In (a), the convergence in time is demonstrated using spatial resolution N=8192. In (b), the convergence study in space is presented. Sample morphologies of the interface at the indicated radii using N=8192 are shown as insets. The initial shape is $r(\alpha,0)=1+0.02(\cos(3\alpha)+\sin(7\alpha)+\cos(15\alpha)+\sin(25\alpha))$, $\tau=1.0\times10^{-5}$, and $b(t)=\exp(t)$.

We next test the resolution in space using N=2048,4096,8192, and 16384 points along the interface. The time step is fixed as $\Delta \bar{t}=4.0\times 10^{-4}$ for all calculations. The error is again measured by the area difference, $Error=|\bar{A}(\bar{t})-\bar{A}(0)|$. Figure 3(b) shows the base 10 logarithm of the space error plotted versus scaling factor. At R=0.69 the run with N=2048 points starts differing from the runs with higher resolutions and then quickly fails. This indicates that more points are needed to resolve the interface. This behavior also occurs at R=0.5 for N=4096. When using N=8192, the results are the same as for N=16384. We notice that while the simulations remain resolved, all these calculations produce almost identical numerical results at the same time, indicating spectral accuracy in space. Four sample morphologies of the interface are shown as insets. The interface evolves to a vanishing circle as it shrinks, and the morphologies with different spatial resolution nearly overlap and are geometrically indistinguishable.

Comparison with the original nonrescaled scheme. To illustrate the efficiency and necessity of our rescaling scheme (especially for small surface tensions that can lead to striking fingering patterns), we set the surface tension to $\tau = 1 \times 10^{-5}$ and the gap to be exponentially increasing $b(t) = \exp(t)$ and compute the dynamics using the original method and then make a contrast with the rescaled scheme where the speed of the gap is reduced to $b(\bar{t}) = 1 + 0.5\bar{t}$. We summarize our simulation results in Figure 4(a). Using N = 4096 mesh points along the interface and the time step $\Delta t = 4 \times 10^{-4}$, the simulation using the original nonscaled method fails at $Q_A(0.48, 1.04)$, where the first coordinate corresponds to the radius and the second to the shape factor. This occurs because N = 4096 does not provide enough grid points to resolve the complex fingering morphology; see the first image in Figure 4(b). Doubling the mesh point only prolongs the simulation to $Q_B(0.3, 1.62)$. Redoubling the spatial resolution does not help the simulation to run further. We then reduce the time step to $\Delta t = 1 \times 10^{-4}$ and find the simulation only extends slightly to $Q_{C}(0.28, 1.71)$, indicating a severe numerical stiffness. An analysis of the morphologies at points Q_A, Q_B, Q_C (shown in Figure 4(b)) reveals that the interface develops small "buds" connected with the bulk fluid via thin necks. To accurately resolve the fluid motion in these narrow regions, the original scheme demands small time steps, as large time steps may result in a crossing of the interface and blow-up of the numerical solution.

To further assess the results, in Figure 4(c) we plot the maximum normal velocity in the original frame $|V|_{max}$ and show the normal velocity in the rescaled frame $|\bar{V}|_{max}$ as an inset. Note that in the rescaled frame, the maximum velocities $|\bar{V}|_{max}$ are smaller than $|V|_{max}$ (computed at the same R in the original scheme). When the normal velocity $|\bar{V}|_{max}$ is mapped back to the original frame, it coincides with the normal velocities from the original scheme before Q_A, Q_B, Q_C where the original scheme fails. After these failure points, the calculations of velocity $|V|_{max}$ lose accuracy and increase rapidly, leading to failed simulations.

However, as shown in Figure 4(a), our rescaling enables one to compute the whole evolution using $\Delta \bar{t} = 4 \times 10^{-4}$ and N = 8192. The reason for such high efficiency is demonstrated in Figure 4(d), where we map the fixed time step $\Delta \bar{t} = 4 \times 10^{-4}$ back to the original time frame following $\Delta t = \ln(1 + \frac{\Delta \bar{t} \bar{R}^2}{2})$. At early growth stages, the equivalent time step in the original (nondimensional) time frame decreases adaptively as the interface shrinks and develops complex fingering patterns. For example, as indicated by the dashed lines in Figure 4(d), at $Q_B(R=0.3)$, the rescaled time step $\Delta \bar{t} = 4 \times 10^{-4}$ equals to $\Delta t = 1.8 \times 10^{-5}$ in the original frame, while at $Q_C(R=0.28)$,

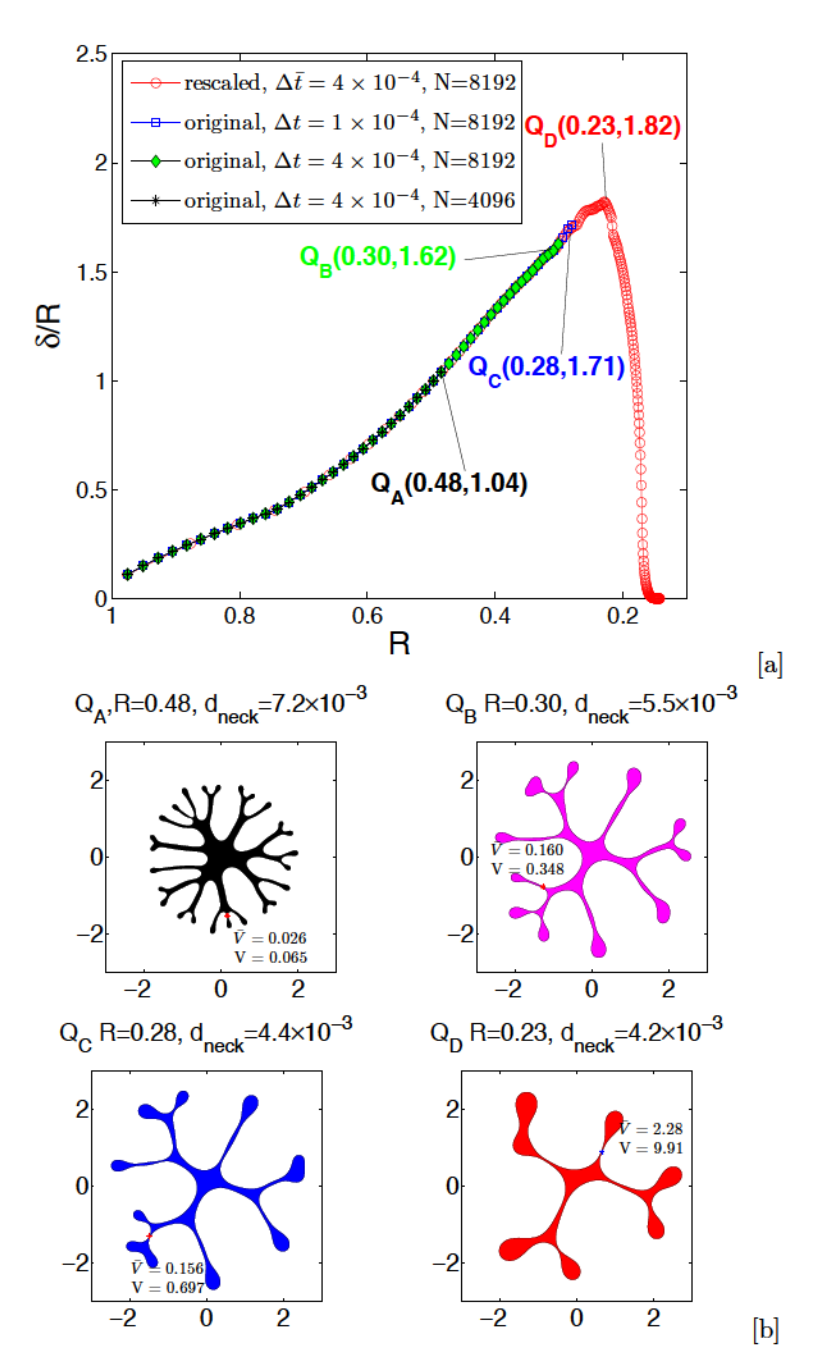


FIG. 4. Interfacial dynamics with an exponentially increasing gap. (a) The nonlinear shape factor $(\frac{\delta}{R})_{NL}$ (see text) using the rescaling scheme (red) and the original scheme using different time and spatial discretization sizes as labeled. Only the rescaled scheme is able to simulate the full evolution, which ultimately tends to a circle as the interface shrinks. (b) Morphologies of the interface at Q_A , Q_B , Q_C , and Q_D using the rescaled scheme. The neck velocity at the red marker point is specified: V in the original frame and \bar{V} in the rescale frame. The initial shape is $r(\alpha,0) = 1 + 0.02(\cos(3\alpha) + \sin(7\alpha) + \cos(15\alpha) + \sin(25\alpha))$, $\tau = 1.0 \times 10^{-5}$, and $b(t) = \exp(t)$.

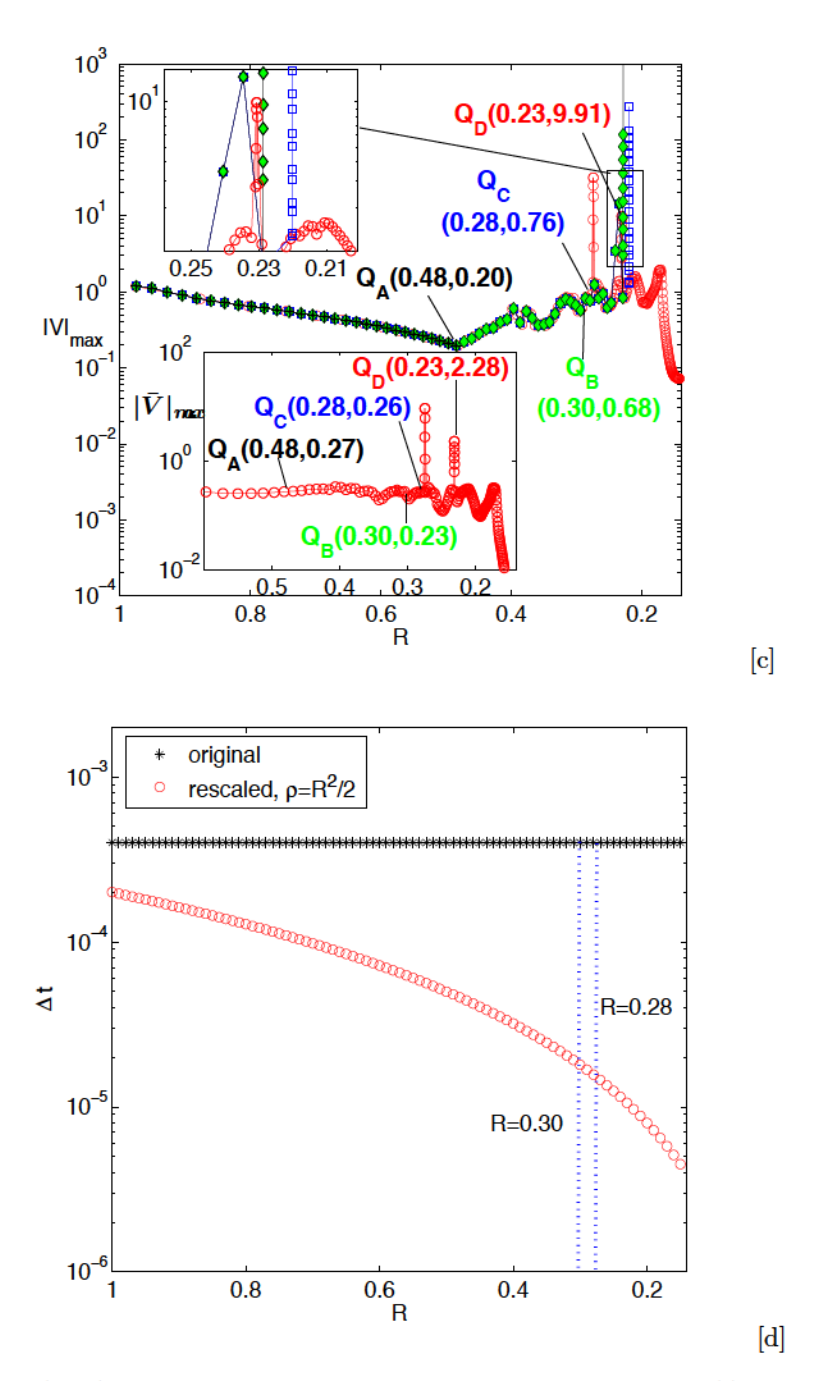


Fig. 4. (cont.). Interfacial dynamics with an exponentially increasing gap. (c) The maximum normal velocity in original frame using rescaled and original schemes (as labeled in (a)). The maximum normal velocity in rescaled frame is shown as an inset. (d) The corresponding time step in original frame for the rescaled scheme (red) and original scheme (black). The vertical dashed lines indicate points at which the time steps for the two schemes are compared. The initial shape is $r(\alpha,0)=1+0.02(\cos(3\alpha)+\sin(7\alpha)+\cos(15\alpha)+\sin(25\alpha)), \ \tau=1.0\times 10^{-5}, \ and \ b(t)=\exp(t).$

the rescaled time step $\Delta \bar{t} = 4 \times 10^{-4}$ is equivalent to $\Delta t = 1.57 \times 10^{-5}$ in the original frame. After the peak point Q_D , although the time step $\Delta \bar{t}$ continues to decrease, the shape factor decays monotonically to a circular shape as the fingers are smoothed out (Figure 4(a)). We note that one may use another time scale function to speed up the calculation in this time period to gain more efficiency, e.g., following the idea in [50].

4.3. Noncircular shrinking shapes. From linear analysis, we know the shape factor of mode k grows fastest when using a gap, $b(t) = \left(1 - \frac{7}{2}ct\right)^{-\frac{2}{7}}$, where $c = 2(3k^2-1)\tau$. The gap remains finite for $t < T_k$, where the critical time $T_k = \frac{1}{7\tau(3k^2-1)}$. As $t \to T_k$, b(t) and $\dot{b}(t)$ blow up rapidly. As a matter of fact, we know from (3.4) that the magnitude of the normal velocity |V| will become infinitely large as R shrinks to zero. Numerically, it is impossible to use the original scheme to simulate the whole shrinking dynamics. We are interested in testing the performance of our algorithm and exploring this superfast dynamics under such a gap. Consequently, we implement a time scaling factor $\rho = R^9/2c$ to slow down this fast evolution such that in the rescaled frame, the gap evolves linearly in time, $b(\bar{t}) = 1 + 0.5\bar{t}$. We set N = 8192 and the time step $\Delta \bar{t} = 1 \times 10^{-4}$. We choose $c = 52\tau$, with $\tau = 1 \times 10^{-4}$, such that mode 3 grows the fastest, or equivalently mode 5 evolves self-similarly, based on linear theory.

We consider three different initial shapes, $r(\alpha, 0) = 1 + 0.02(\cos(3\alpha) + \sin(7\alpha) + \cos(3\alpha))$ $\cos(15\alpha) + \sin(25\alpha)$, $r(\alpha, 0) = 1 + 0.02(\sin(6\alpha) + \cos(15\alpha) + \sin(25\alpha))$, and $r(\alpha, 0) = 0$ $1+0.02(\cos(3\alpha)+\cos(5\alpha)+\cos(6\alpha))$ (labeled respectively first, second, and third). In Figure 5(a), we plot the shape factor against the interface size R for each simulation and two sequences of the morphologies are shown as insets, with the upper and lower plots corresponding to the first and second initial conditions, respectively. We notice that the interface morphologies are eventually dominated by mode 3 for all simulations as the interface shrinks. The sequence of morphologies using the third initial shape is shown in Figure 5(b). As the interface shrinks, the shapes exhibit the three long thin channels with three tiny "buds" at the tip of each channel. In Figure 5(c), we show the normal velocities at the tip of the "bud" (marked by O_A in Figure 5(b)) and the inner end of a channel (marked by O_B in Figure 5(b)) as a function of R. As R decreases to zero, the normal velocity in the original frame goes unbounded. However, in the rescaled frame (shown as an inset) the normal velocity decreases and tends to zero (albeit with an infinite slope). In practice, we find our simulations stop approximately at $T_3 - t \approx 2 \times 10^{-11}$. Note that while the interface shrinks, the size of the "bud" keeps decreasing, as evidenced by the fact that the curvature becomes unbounded as shown in Figure 5(d). In addition, we find the neck width also decreases and the thin channel keeps being stretched even thinner.

For the simulation using the initial shape $r(\alpha,0) = 1 + 0.02(\sin(6\alpha) + \cos(15\alpha) + \sin(25\alpha))$, in which mode 3 is not included initially, the nonlinear interactions among the existing modes eventually create mode 3. From Figure 5(a), we observe the shape factor actually decreases until mode 3 is created at $R \approx 0.16$. Therefore, this specific gap dynamics selects mode 3 as the fastest growth mode and drives the interface to a symmetric threefold pattern. Unlike an expanding interface, for which the interaction among modes introduces nonlinear stabilization and leads the interface to nonlinear dynamical equilibrium states (nonlinear self-similar evolution [29, 30, 28])), here we do not observe any nonlinear self-similar evolution. This may be because unlike the expanding case, there is insufficient time for the system to lock on to a stable nonlinear self-similar shape before the radius of the drop vanishes at a finite time. However, what is apparent from our simulations is that there is mode selection during the nonlinear dynamics. We cannot rule out that there may be special nonlinear, stable

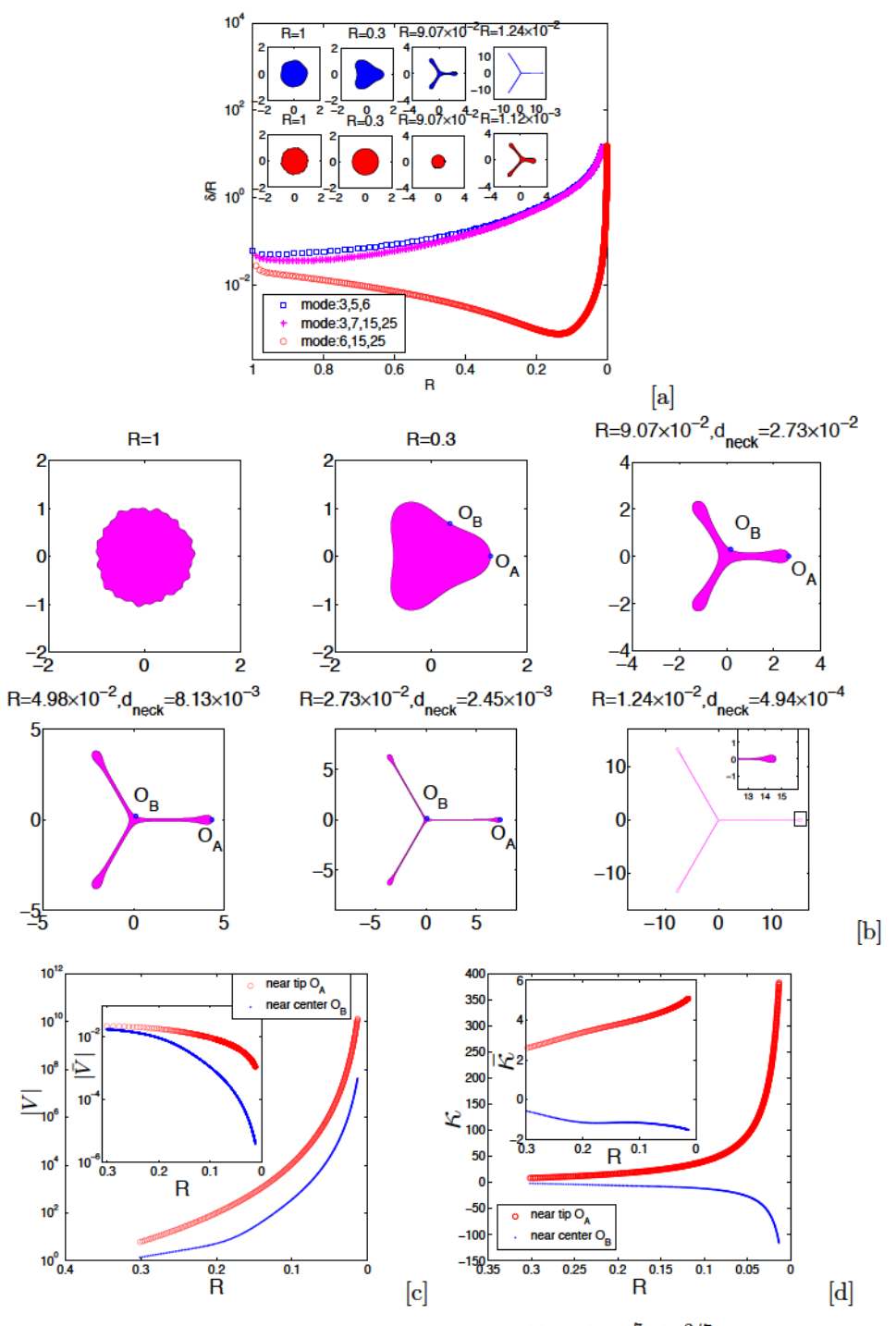


Fig. 5. Interfacial dynamics under the special gap $b(t)=(1-\frac{7}{2}ct)^{-2/7}$ where c is chosen such that k=3 is the fastest growing linear mode (see text). (a) The evolution of the nonlinear shape factor for three different initial conditions (see text); the insets show the morphologies from the first two initial conditions at the indicated radii. (b) The simulated interfacial morphologies during shrinkage for the third initial condition. (c) The normal velocity in the original frame |V| at O_A and O_B in original frame (see (b)) and the normal velocity in the rescaled frame |V| is shown as an inset. (d) The curvature of the shrinking threefold shape at O_A and O_B . Surprisingly, the interface does not shrink like a circle but rather as a one-dimensional slender rod-like morphology with a threefold symmetry (see Figure 6).

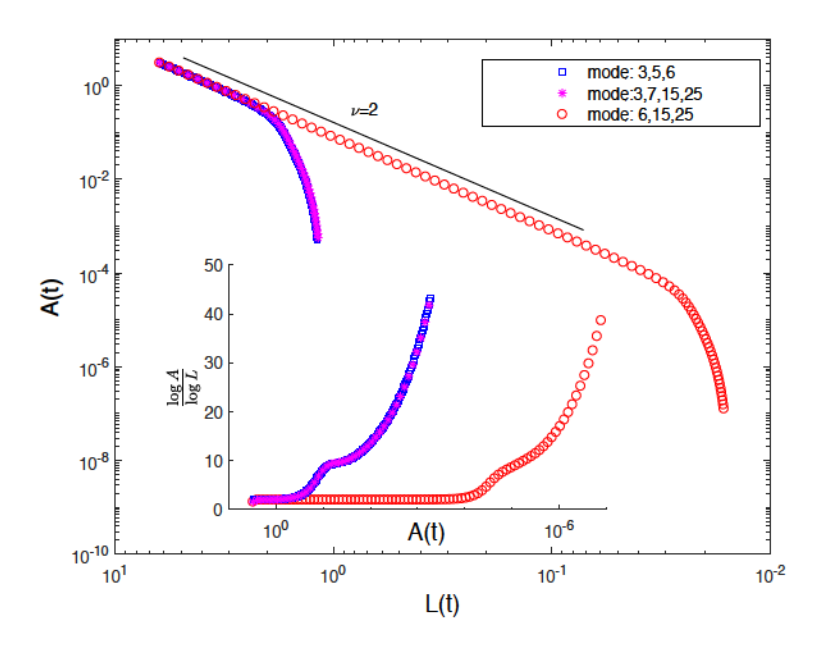


FIG. 6. Scaling characteristics of the interface from Figure 5: the relation between the enclosed area A(t) and perimeter L(t) of the interface in the original, unscaled frame. When the interface is compact, $A \sim L^{\nu}$ with $\nu = 2$. As the interface shrinks, ν increases as shown in the inset, which indicates that the area shrinks much faster than the length.

self-similar shrinking interfaces such as those observed in [9, 10] when a bubble is driven to extinction by the presence of a sink in a Hele-Shaw cell.

In Figure 6, we show a relation between the enclosed area A(t) and the perimeter L(t) as $A(t) \sim L^{\nu}(t)$. Both the area and the perimeter are measured in the original (nondimensional) time frame. At early times, when the interface is compact, we have $A(t) \sim L^2(t)$, e.g., $\nu = 2$ as expected. At later times, we see all three curves decrease rapidly as the interface develops a mode 3 dominated geometry. In particular, the value of ν goes up to 45 as shown in the inset, indicating the area A shrinks much faster than the perimeter, though both A(t) and L(t) decrease monotonically (not shown).

4.4. Dynamics of a fission interface. In [43], the authors constructed an interface that would fission into two distinct interfaces under zero surface tension. The general shape is given by $(x_1^2 + x_2^2)^2 = \frac{4\eta x_1^2}{(1-\omega_0^2)^2} + \frac{4\eta x_2^2}{(1+\omega_0^2)^2}$, where $\eta = \frac{1-\omega_0^4}{2\omega_0} R_f$, $\omega_0 = \sqrt{\frac{b(t)}{b(0)}} - \sqrt{(\frac{b(t)}{b(0)})^2 - 1}$, and R_f is the radius of the circle when the fission occurs. Using the parameters $\eta = \frac{15}{16}$, $\omega_0 = 1/2$, $R_f = 1$, and $b(t) = \exp(t)$, the analytical

Using the parameters $\eta = \frac{10}{16}$, $\omega_0 = 1/2$, $R_f = 1$, and $b(t) = \exp(t)$, the analytical solution suggests the interface pinches off into two separate circles with radius 1 at $t_f = 0.75$ [43].

Here we are interested in exploring the long-time nonlinear dynamics under a small

surface tension. We use the parameters listed above and take the surface tension $\tau=2\times 10^{-5}$. Thus the initial shape is $(x_1^2+x_2^2)^2=\frac{25x_1^2}{4}+\frac{9x_2^2}{4}$ or $r(\alpha,0)=\sqrt{\frac{9}{4}+4\cos^2(\alpha)}$. We use N=8192 points along the interface and rescale time such that in the rescaled frame $b(\bar{t})=1+0.5\bar{t}$. The time step is $\Delta \bar{t}=2\times 10^{-4}$.

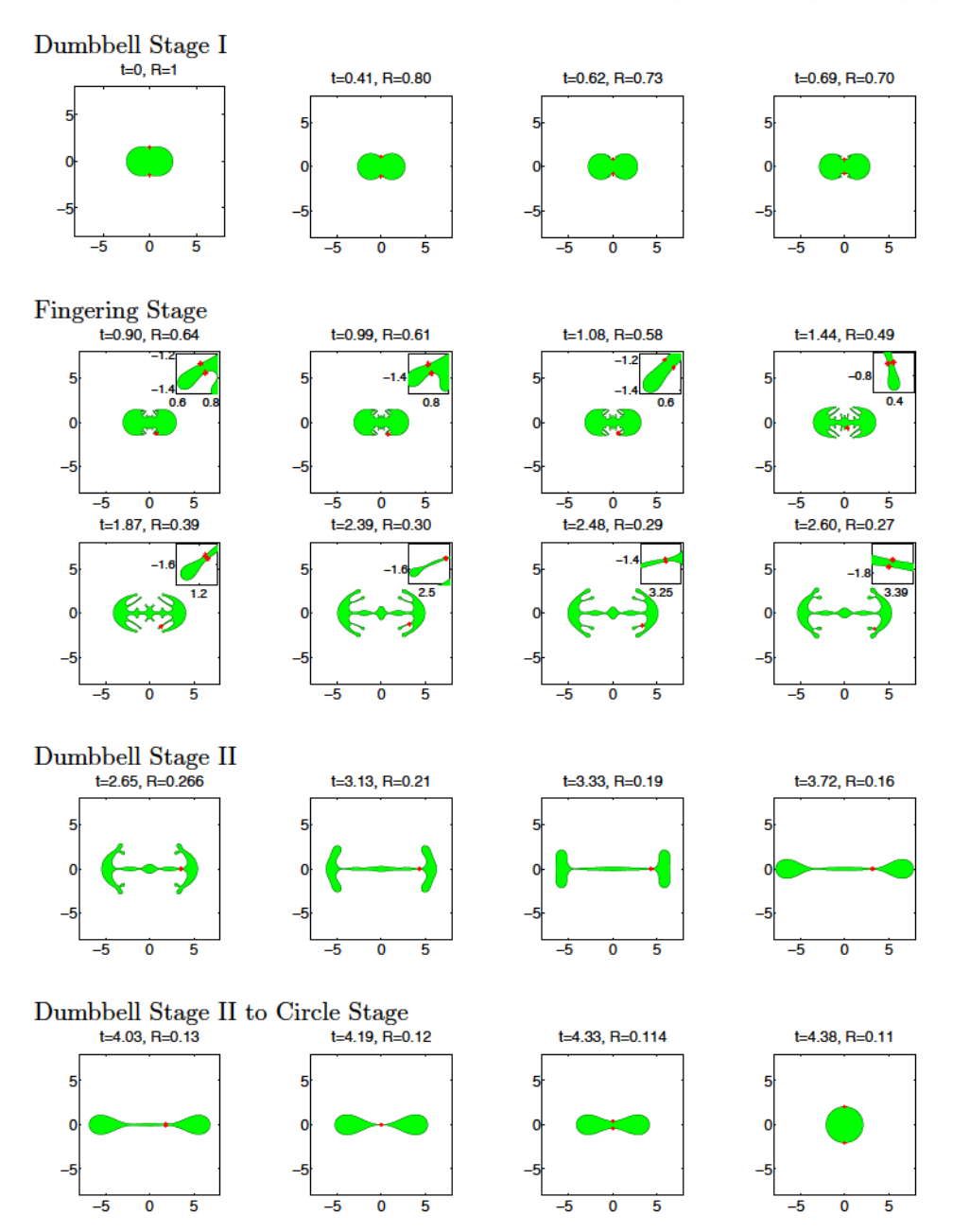


Fig. 7. The dynamics of an interface that would fission into two circles at the original (unscaled) nondimensional time t=0.75 if the surface tension $\tau=0$ and the gap exponentially increases (see text). Here, the surface tension is small but finite ($\tau=2\times 10^{-5}$). The scaled interfacial morphologies (same area) are shown as a function of the original time and R as labeled. Note the development of fingers in the neck region and a long neck that separates two bulbs of fluid. Eventually though the interface shrinks as a circle. There are four stages of the dynamics: 1. a dumbbell stage; 2. a fingering stage; 3. a dumbbell stage; and 4. a circle stage (see text and Figure 8). The red points of each plot are the locations where the interfacial necks are narrowest.

In Figure 7, we show a time sequence of the evolution in the rescaled frame (the original times are shown along with R). The red stars in each plot are the points

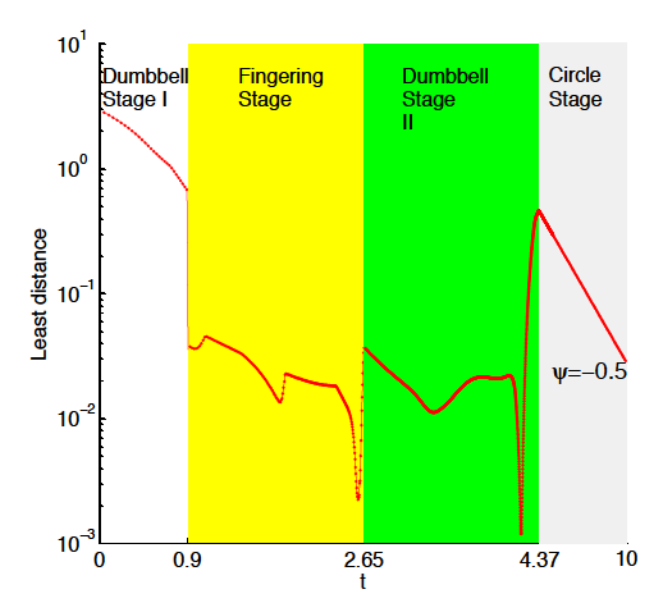


FIG. 8. The minimum distance between interfacial necks from the simulation in Figure 7 during the four stages of the dynamics, as labeled. The results are presented in the original, unscaled frame.

used to compute the least distance between interfacial necks measured in the original frame (defined later). We observe the interface experiences a four-stage evolution. During Dumbbell Stage I (the first row of Figure 7), the interface develops two near circular buds connected by a flat channel. Small fingers appear around the channel regions when the size of the interface shrinks to $R \approx 0.7$. During this stage, we define the least distance as the width at the center of the channel region (x = 0). As the interface continues to shrink, the dynamics transits into the Fingering Stage (eight snapshots are shown in the second and third rows of Figure 7). We observe that more fingers appear on both the buds and the channel, while the channel gets thinner. We define the least distance as the minimum width of a fjord (shown as an inset in each snapshot). In fact, the least distance measures the neck width of a fjord. Because the least distance is defined differently for each stage, the least distance curve in Figure 8 shows a jump at the transition time. During the Fingering Stage, the fingers show remarkable growth. At the end of this stage, most fingers decay and the neck width of a fjord is comparable to the width of the channel. The interface then enters Dumbbell Stage II, at which the least distance is again measured by the neck width of the channel. During this stage, the fingers continue to decay and the two buds are connected by a very thin channel. The least distance positions are located near the connection region between the bud and the channel. As R continues to shrink, this position moves back to the center of the channel region (x = 0). Linear theory also predicts all modes decay at $t^* = 3.20$ during Dumbbell Stage II. At the Circle Stage, the two buds merge into one and the least distance is the diameter of the circle. In Figure 8, we notice the least distance reaches a local minimum $d_{min} = 2.36 \times 10^{-3}$ at t = 2.59 (the neck width of a fjord), and another local minimum $d_{min} = 1.20 \times 10^{-3}$ at t = 4.19 (the width of the channel center). Once the system enters the Circle Stage, R shrinks exponentially fast $R \sim e^{-\Psi t}$ with $\Psi = -0.5$.

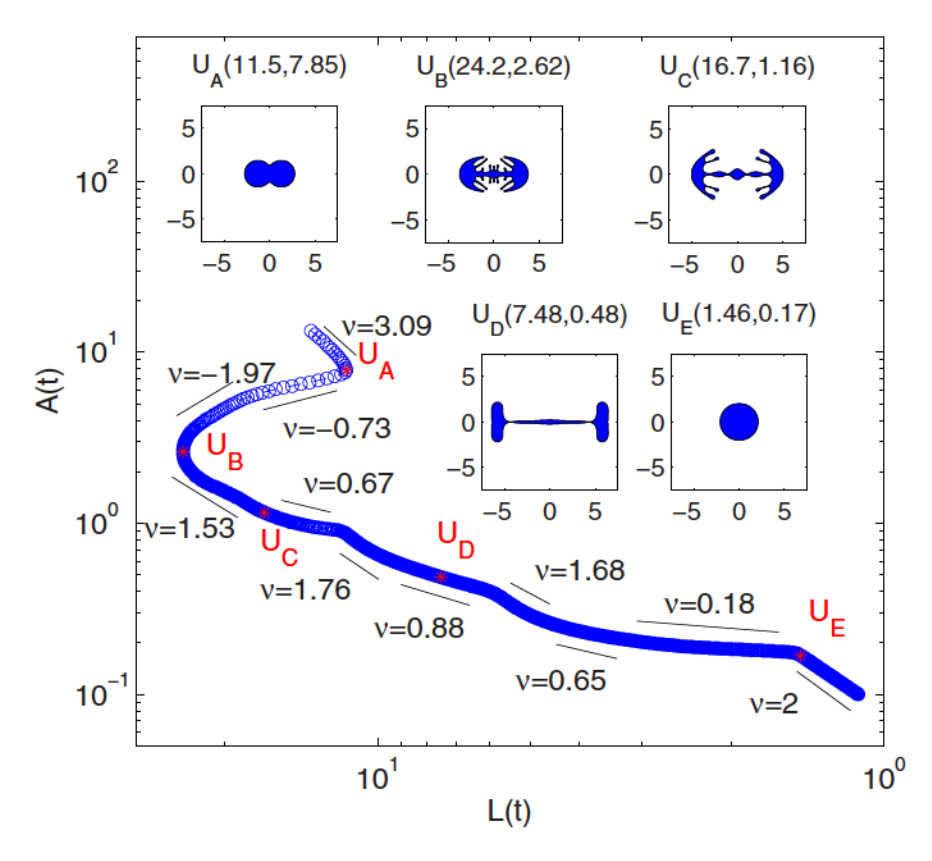


Fig. 9. Scaling of the interface from Figure 7. It shows that the relation between A(t) and L(t) is highly dynamic.

Figure 9 shows the relation between the area A(t) and the arclength L(t), $A(t) \sim L^{\nu}(t)$. The relationship is dynamic. From the beginning to point $U_A(L=11.5, A=7.85)$, the viscous fluid stays in a compact shape, $A(t) \sim L^{3.09}(t)$. After U_A , L(t) turns to grow, while A(t) continues to decay, and the scaling parameter changes from $\nu = -0.73$ to $\nu = -1.97$. The interface experiences multiple fingers. At $U_B(L=24.2, A=2.62)$, L(t) reaches its maximum there and a transition occurs. After this point, both A(t) and L(t) decay. The scaling parameter ν decreases from 1.53 to 0.67. The second transition occurs at (L=11.75, A=0.89). The scaling parameter ν decreases from 1.76 to 0.88 as most fingers are smoothed out and the compact buds tend to be formed. Later at (L=5.89, A=0.39), the third transition occurs, where the scaling parameter ν decreases from 1.68 to 0.65 and then 0.18, as the buds tend to merge. After $U_E(L=1.46, A=0.17)$, the interface evolves as a vanishing circle.

5. Conclusion. In this paper, we have studied the Hele-Shaw problem with a time increasing gap b(t). Using linear theory, we have shown that for a special choice of the gap $b(t) = \left(1 - \frac{7}{2}ct\right)^{-\frac{2}{7}}$, with $c \sim k^2$ where k is a wavenumber, the interface separating an inner viscous fluid from air can evolve self-similarly with k-fold symmetry using one choice of c or that mode k is the fastest growing wavenumber using another choice of c. For other choices of gap widths, such as linearly or exponentially increasing time dependent gaps, there exists a critical time after which shape perturbations start to decay.

We have implemented a boundary integral method with spatial temporal rescaling to simulate the nonlinear dynamics of the interface. As the interface shrinks, a small time step is needed [43, 31], especially when the size of the interface is small. We implement rescaling to slow down the evolution speed of the interface in the rescaled frame such that this time step constraint can be removed. Though the time step Δt is fixed in the rescaled frame, the equivalent time step Δt in the original frame decreases adaptively via the time scaling function. Our results demonstrate that the new rescaling algorithm is capable of accurately simulating the interface dynamics for far longer times of the evolution than could be done previously. In particular, when we used the gap $b(t) = \left(1 - \frac{7}{2}ct\right)^{-\frac{2}{7}}$ such that mode k = 3 is fastest growing according to linear theory, we found that rather than shrinking like a circle, the interface acquires a one-dimensional slender rod-like geometry with a threefold symmetry as it vanishes.

We also studied a fissioning interface under an exponentially increasing gap $b(t) = \exp(t)$ using a small surface tension. The evolution exhibits four stages of dynamics. During Dumbbell Stage I (Stage 1), the interface develops few fingers and remains compact with the appearance of two buds connected by a thin channel. During the Fingering Stage (Stage 2), the interface develops long fingers on both of the buds and the channel connecting them. During Dumbbell Stage II (Stage 3), fingers decay and the interface evolves into two buds which attract each other and merge. During the Circle Stage (Stage 4), the interface tends to a circle as it vanishes. Our simulation shows the interface does not separate, which is different from the zero surface tension solution [43] and the lubrication approximation [1]. Thus, surface tension here provides a smoothing effect that prevents the occurrence of these morphological singularities. However, we do not rule out the possibility that there may be initial conditions that could lead to pinch-off [7, 15], but this is beyond the scope of our paper.

In the future, we plan to perform a more complete investigation into the dynamics of shrinking interfaces in a Hele-Shaw cell. In particular, following our prior work [28], we plan to develop a morphology diagram of shrinking interface shapes as a function of c when the gap $b(t) = \left(1 - \frac{7}{2}ct\right)^{-\frac{2}{7}}$ is used. We also plan to further investigate the fissioning interface to determine the behavior in the limit as the surface tension $\tau \to 0$. We plan to study the singularities formed due to a small surface tension solution [44] and understand the coupling/competition effect between the surface tension and the driving force introduced by the increasing gap.

REFERENCES

- R. Almgren, Singularity formation in Hele-Shaw bubbles, Phys. Fluids, 8 (1996), pp. 344-352.
- [2] M. B. AMAR AND D. BONN, Fingering instabilities in adhesive failure, Phys. D, 209 (2005), pp. 1–16.
- [3] E. Ben-Jacob, G. Deutscher, P. Garik, N. Goldenfeld, and Y. Lareah, Formation of a dense branching morphology in interfacial growth, Phys. Rev. Lett., 57 (1986), pp. 1903– 1906
- [4] G. CARVALHO, H. GADÊLHA, AND J. MIRANDA, Elastic fingering in rotating Hele-Shaw flows, Phys. Rev. E, 89 (2014), 053019.
- [5] C.-Y. CHEN, C.-H. CHEN, AND J. MIRANDA, Numerical study of miscible fingering in a timedependent gap Hele-Shaw cell, Phys. Rev. E, 71 (2005), 056304.
- [6] R. CHUOKE, P. V. MEURS, AND C. V. DER POEL, The instability of slow immiscible viscous liquid-liquid displacements in permeable media, Trans. AIME, 216 (1959), pp. 188–194.
- [7] P. CONSTANTIN, T. DUPONT, R. GOLDSTEIN, L. KADANOFF, M. SHELLEY, AND S. ZHOU, Droplet breakup in a model of the Hele-Shaw cell, Phys. Rev. E, 47 (1993), 4169.
- [8] H. CUMMINS, L. FOURTUNE, AND M. RABAUD, Successive bifurcations in directional viscous fingering, Phys. Rev. E, 47 (1993), pp. 1727–1738.

- [9] M. DALLASTON AND S. MCCUE, Bubble extinction in Hele-Shaw flow with surface tension and kinetic undercooling regularization, Nonlinearity, 26 (2013), pp. 1639–1665.
- [10] M. DALLASTON AND S. MCCUE, A curve shortening flow rule for closed embedded plane curves with a prescribed rate of change in enclosed area, Proc. A, 472 (2016), 20150629.
- [11] D. DERKS, A. LINDNER, C. CRETON, AND D. BONN, Cohesive failure of thin layers of soft model adhesives under tension, J. App. Phys., 93 (2003), pp. 1557–1566.
- [12] E. DIAS AND J. MIRANDA, Control of radial fingering patterns: A weakly nonlinear approach, Phys. Rev. E, 81 (2010), 016312.
- [13] E. DIAS AND J. MIRANDA, Determining the number of fingers in the lifting Hele-Shaw problem, Phys. Rev. E, 88 (2013), 043002.
- [14] E. DIAS AND J. MIRANDA, Taper-induced control of viscous fingering in variable-gap Hele-Shaw flows, Phys. Rev. E, 87 (2013), 053015.
- [15] T. DUPONT, R. GOLDSTEIN, L. KADANOFF, AND S. ZHOU, Finite-time singularity formation in Hele-Shaw systems, Phys. Rev. E, 47 (1993), 4182.
- [16] B. Francis and R. Horn, Apparatus-specific analysis of fluid adhesion measurements, J. Appl. Phys., 89 (2001), pp. 4167–4174.
- [17] S. GOLDSTEIN, Modern Developments in Fluid Dynamics, Oxford University Press, Oxford, UK, 1938.
- [18] A. GREENBAUM, L. GREENGARD, AND G. B. McFADDEN, Laplace's equation and the Dirichlet-Nuemann map in multiply connected domains, J. Comput. Phys., 105 (1993), pp. 267–278.
- [19] L. GREENGARD AND V. ROKHLIN, A fast algorithm for particle summations, J. Comput. Phys., 73 (1987), pp. 325–348.
- [20] H. Guo, D. Hong, and D. Kurtze, Surface-tension-driven nonlinear instability in viscous fingers, Phys. Rev. Lett., 69 (1992), pp. 1520-1523.
- [21] A. HE, J. LOWENGRUB, AND A. BELMONTE, Modeling an elastic fingering instability in a reactive Hele-Shaw flow, SIAM J. Appl. Math., 72 (2012), pp. 842–856.
- [22] T. Hou, J. Lowengrub, and M. Shelley, Removing the stiffness from interfacial flows with surface tension, J. Comput. Phys., 114 (1994), pp. 312-338.
- [23] T. HOU, J. LOWENGRUB, AND M. SHELLEY, The long-time motion of vortex sheets with surface tension, Phys. Fluids, 9 (1997), pp. 1933–1954.
- [24] T. Hou, J. Lowengrub, and M. Shelley, Boundary integral methods for multicomponent fluids and multiphase materials, J. Comput. Phys., 169 (2001), pp. 302–362.
- [25] H. LAKROUT, P. SERGOT, AND C. CRETON, Direct observation of cavitation and fibrillation in a probe tack experiment on model acrylic pressure-sensitive-adhesives, J. Adhes., 69 (1999), pp. 307-359.
- [26] H. Lamb, Hydrodynamics, Cambridge University Press, Cambridge, UK, 1932.
- [27] S. Li and X. Li, A boundary integral method for computing the dynamics of an epitaxial island, SIAM J. Sci. Comput., 33 (2011), pp. 3282-3302.
- [28] S. LI, J. LOWENGRUB, J. FONTANA, AND P. PALFFY-MUHORAY, Control of viscous fingering patterns in a radial Hele-Shaw cell, Phys. Rev. Lett., 102 (2009), 174501.
- [29] S. Li, J. Lowengrub, and P. Leo, A rescaling scheme with application to the long-time simulation of viscous fingering in a Hele-Shaw cell, J. Comput. Phys., 225 (2007), pp. 554-567.
- [30] S. Li, J. Lowengrub, P. Leo, and V. Cristini, Nonlinear theory of self-similar crystal growth and melting, J. Crystal Growth, 267 (2004), pp. 703-713.
- [31] A. LINDNER, D. DERKS, AND M. SHELLEY, Stretch flow of thin layers of Newtonian liquids: Fingering patterns and lifting forces, Phys. Fluids, 17 (2005), 072107.
- [32] G. McKinley and T. Sridhar, Filament-stretching rheometry of complex fluids, Ann. Rev. Fluid Mech., 34 (2002), pp. 375-415.
- [33] J. McLean and P. Saffman, The effect of surface tension on the shape of fingers in a Hele-Shaw cell, J. Fluid Mech., 102 (1981), pp. 455-469.
- [34] W. Mullins and R. Sekerka, Morphological stability of a particle growing by diffusion or heat flow, J. Appl. Phys., 34 (1963), pp. 323-329.
- [35] J. NASE, D. DERKS, AND A. LINDNER, Dynamic evolution of fingering patterns in a lifted Hele-Shaw cell, Phys. Fluids, 23 (2011), 123101.
- [36] C. Park, S. Gorell, and G. Homsy, Two-phase displacement in Hele-Shaw cells: experiments on viscously driven instabilities, J. Fluid Mech., 141 (1984), pp. 257–287.
- [37] T. PODGORSKI, M. SOSTARECZ, S. ZORMAN, AND A. BELMONTE, Fingering instabilities of a reactive micellar interface, Phys. Rev. E, 76 (2007), 016202.
- [38] S. POIVET, F. NALLET, C. GAY, AND P. FABRE, Cavitation-induced force transition in confined viscous liquids under traction, Europhys. Lett., 62 (2003), pp. 244–250.
- [39] O. PRAUD AND H. SWINNEY, Fractal dimension and unscreened angles measured for radial viscous fingering, Phys. Rev. E, 72 (2005), 011406.

- [40] L. Reis and J. Miranda, Controlling fingering instabilities in nonflat Hele-Shaw geometries, Phys. Rev. E, 84 (2011), 066313.
- [41] Y. SAAD AND M. SCHULTZ, GMRES: A generalized minimal residual algorithm for solving nonsymmetric linear systems, SIAM J. Sci. Statist. Comput., 7 (1986), pp. 856–869.
- [42] P. SAFFMAN AND G. TAYLOR, The penetration of a fluid into a porous medium or a Hele-Shaw cell containing a more viscous fluid, Proc. A, 245 (1958), pp. 312-329.
- [43] M. SHELLEY, F. TIAN, AND K. WLODARSKI, Hele-Shaw flow and pattern formation in a timedependent gap, Nonlinearity, 10 (1997), pp. 1471-1495.
- [44] M. SIEGEL, S. TANVEER, AND W. DAI, Singular effects of surface tension in evolving Hele-Shaw flows, J. Fluid Mech., 323 (1996), pp. 201–236.
- [45] S. SINHA, T. DUTTA, AND S. TARAFDAR, Adhesion and fingering in the lifting Hele-Shaw cell: Role of the substrate, Eur. Phys. J. E, 25 (2008), pp. 267-275.
- [46] S. Sinha and S. Tarafdar, Viscous fingering patterns and evolution of their fractal dimension, Ind. Eng. Chem. Res., 48 (2009), pp. 8837–8841.
- [47] A. TATULCHENKOV AND A. CEBERS, Magnetic fluid labyrinthine instability in Hele-Shaw cell with time dependent gap, Phys. Fluids, 20 (2008), 054101.
- [48] S.-Z. ZHANG, E. LOUIS, O. PLA, AND F. GUINEA, Linear stability analysis of the Hele-Shaw cell with lifting plates, Eur. Phys. J. B, 1 (1998), pp. 123-127.
- [49] M. Zhao, A. Belmonte, S. Li, X. Li, and J. Lowengrub, Nonlinear simulations of elastic fingering in a Hele-Shaw cell, J. Comput. Appl. Math., 307 (2016), pp. 394-407.
- [50] M. Zhao, W. Yin, J. Lowengrub, and S. Li, An efficient adaptive rescaling scheme for computing moving interface problems, Commun. Comput. Phys., 21 (2017), pp. 679–691.
- [51] A. Zosel, Adhesion and tack of polymers: Influence of mechanical properties and surface tensions, Colloid. Polym. Sci., 263 (1985), pp. 541–553.